GSA Data Repository 2017068

The origin of contractional structures in extensional gneiss domes

P. F. Rey[1], L. Mondy[1], G. Duclaux[2], C. Teyssier[3], D. L. Whitney[3], M. Bocher[4], C. Prigent [5]

SUPPLEMENTAL FILES

Rheology: For frictional rheology we use a yield stress that increases linearly with depth according to: $\tau < C_0 + \mu \cdot \sigma_n$ with τ the second invariant of the deviatoric stress tensor; C_0 the cohesion; σ_n the lithostatic pressure; and μ the coefficient of friction. This frictional rheology is modulated via a strain weakening term, which reduces the cohesion and the friction coefficient (Table DR1). A stress- and temperature-dependent flow law, with imposed cut-off viscosities (10^{18} and 10^{24} Pa.s), simulates incompressible viscous flow. The flow parameters are taken from experimental rheology of wet olivine for the mantle, quartz-rich rocks representative of the upper crust, and mafic granulites for the lower crust (Table DR1). When temperature exceeds a rock's solidus, the melt fraction reduces the viscosity (e.g. Rosenberg and Handy, 2005). Hence, in our experiments, the viscous rheology is modulated by a term that takes into account the presence of partial melt.

2017068_A_MCC230_Input_40km.zip

2017068_MCC200_Input_60km.zip

TABLE DR1. THERMAL AND MECHANICAL PARAMETERS

Parameters	**Upper crust**[a]	**Lower crust**[b]	**Fault**[c]	**Lithospheric mantle**[d]	**Asthenosphere**[f]
Rheological parameters					
Pre-exponential factor (MPa^{-n}s^{-1})	6.6069e-8	0.1	5e-6	1600	N.A.
Activation Energy (kJ.mol^{-1})	135	244	190	520	N.A.
Stress exponent	3.1	3.2	3	3.5	N.A.
Water fugacity	0	0	0	1000	N.A.
Water fugacity exponent	0	0	0	1.2	N.A.
Activation volume (m^3.mol^{-1})	0	0	0	23e-6	N.A.
Reference density (kg m^{-3})	2800	2900	2800	3300	3360
Cohesion (MPa)	10	10	5	10	10
Cohesion after softening (MPa)	2	4	1	2	2
Coefficient of friction	0.577	0.577	0.134	0.577	0.577
Softened coeff. of friction	0.115	0.115	0.0134	0.115	0.115
Saturation strain[g]	0.2	0.2	0.2	0.2	0.2
Melt softening factor	1.0e-3	1.0e-3	1.0e-3	1.0e-3	1.0e-3
Softening melt fraction	0.2-0.3	0 - 0.3	0 - 0.3	0.01-0.08	0.01-0.08

[a] Upper crust rheology is based on quartzite rheology (Paterson and Luan, 1990).

[b] Fault rheology is based on wet quartzite rheology (Brace and Kohlstedt, 1980).

[c] Lower crust rheology is based on mafic granulite (Wang et al., 2012)

[d] Lithospheric mantle rheology is based on wet olivine (Hirth et a., 2003)

[f] Asthenosphere has a constant viscosity of 1e20 Pa.s

[g] Saturation strain is the maximum cumulative strain at which softening reaches its minimum value

TABLE DR1 cont.

Parameters	**Upper crust**	**Lower crust**	**Fault**	**Lithospheric mantle**	**Asthenosphere**
Thermal parameters					
Thermal expansivity (K^{-1})	3e-5	3e-5	3e-5	3e-5	3e-5
Heat capacity ($J\ K^{-1}\ kg^{-1}$)	1000	1000	1000	1000	1000
Thermal diffusivity ($m^2\ s^{-1}$)	1.0e-6	1.0e-6	1.0e-6	1.0e-6	1.0e-6
Latent heat of fusion ($kJ\ kg^{-1}$)	300	300	300	300	300
Radiogenic heat ($W\ m^{-3}$)	1.2e-6	0.6e-6	1.2e-6	0.02e-6	0
Density change upon melting (%)[h]	13	13	13	13	13
Solidus[i] a_0 (K)	993	993	993	1393	1393
Solidus a_1 ($K\ Pa^{-1}$)	-1.2e7	-1.2e7	-1.2e7	1.329e-7	1.329e-7
Solidus a_2 ($K\ Pa^{-2}$)	1.2e16	1.2e16	1.2e16	-5.104e-18	-5.104e-18
Liquidus b_0 (K)	1493	1493	1493	2013	2013
Liquidus b_1 ($K\ Pa^{-1}$)	-1.2e7	-1.2e7	-1.2e7	6.15e-8	6.15e-8
Liquidus b_2 ($K\ Pa^{-2}$)	1.6e16	1.6e16	1.6e16	3.12e-18	3.12e-18

[h] Melt fraction is calculated following McKenzie and Bickle, (1988). The density of partially melted rocks decreases linearly with the melt fraction.

[i] Solidus and liquidus are defined by a polynomial function of pressure (P): $T_s = a_0 + a_1 \times P + a_2 \times P^2$, $T_l = b_0 + b_1 \times P + b_2 \times P^2$

Figure DR1: Evolution of fault patterns in the pull-apart region for both the decoupled (A) and coupled (B) models. Faults have a grey shading on the SW-NE and E-W cross-sections (cf. inset). On both coupled and decoupled experiments steeply dipping extensional fractures sub-perpendicular to the direction of plate motion evolve into normal faults dissecting the pull-apart region into fault-bounded blocks.

Figure DR2: Strain fields for the coupled model. A/ Maps of the topographic surface showing evolution of brittle faults (black lines) through times. B/ Ductile strain field and flow field at 6 m.y.: B_1/ 3D view of the model showing the location of the cross-section in panel B_2. The Moho surface is colored for elevation (blue is 40 km depth; brown is 26 km depth). Strain markers at the Moho, initially spherical, are in dark grey. B_2/ Cross-section showing deformed strain markers in the lower crust, and foliation trajectories (dashed lines). Strain markers are colored for strain rate. B_3/ Forward streamlines starting on a series of point initially distributed along a horizontal NW-SE diagonal at 38 km depth in the lower crust. Streamlines are colored for elevation. They are broadly aligned with the direction of plate motion. Grey arrows show the velocity vectors at 38 km depth within the lower crust. C/ Velocity streamlines for the coupled (C_1) and decoupled models (C_2) at 6 m.y. In both cases streamlines start in the lower crust.

Figure DR3: Finite strain markers in the coupled model at 6.7 m.y. A/ Various views of finite strain markers initially 2 km above the Moho (i.e. 38 km depth). Color shows the topography of the Moho. B/ Various views of finite strain markers initially located at the top of the lower crust (20 km depth). Color shows the topography of the top of the lower crust.

Figure DR4: Assessing exhumation of the deep crust in the decoupled experiment (i.e. crustal thickness of 60 km). A/ Distribution at $t = t_0\ yr$ of a set of regularly spaced spherical strain markers (radius 1.5 km) each located at 54 km depth. Each sphere consists in 2000 passive tracers homogeneously distributed at its surface. The deformation of these spheres documents the evolving shape and magnitude of the finite strain. B/ Snapshot at $t = t_0 + 6.7\ m.y.$ showing deformed spheres initially located at 42 km (B_1) and 54 km depth (B_2). The color of each individual tracer is a function of its depth. In the shallow part of the dome, rocks at depth between 4.4 and 1.8 km originate from the deeper crust at depth between 42 and 54 km; a decompression of ~1000 MPa in 6.7 m.y.

REFERENCES CITED

Brace, W.F., and Kohlstedt, D.L., 1980, Limits on lithospheric stress imposed by laboratory experiments: Journal of Geophysical Research, v. 85, p. 6248-6252, doi:10.1029/JB085iB11p06248.

Hirth, G., and Kohlstedt, 2003, Rheology of the upper mantle and the mantle wedge: a view from the experimentalists. *In* Eiler, J, ed., Inside the Subduction Factory: Geophysical Monograph, American Geophysical Union, Washington DC, p. 83-105.

McKenzie, D.R, and Bickle, M.J., 1988, The volume and composition of melt generation by extension of the lithosphere: Journal of Petrology, v. 29, p. 625-679, doi:10.1093/petrology/29.3.625.

Paterson, M.S., and Luan, F.C., 1990, Quartzite rheology under geological conditions, *in* Knipe, R.J, and Rutter, E.H., eds., Deformation Mechanisms, Rheology and Tectonics: London, Geological Society, London, Special Publication 54, p. 299-307.

Rosenberg, C. L., and Handy, M. R., 2005, Experimental deformation of partially melted granite revisited: implications for the continental crust. Journal of Metamorphic Geology, v. 23, p. 19–28, doi:10.1111/j.1525-1314.2005.00555.x.

Wang, Y.F, Zhang, J.F., Jin, Z.M., and Green, H.W., 2012, Mafic granulite rheology: Implications for a weak continental lower crust: Earth and Planetary Science Letters, v. 353-354, p. 99-107, doi:10.1016/j.epsl.2012.08.004.

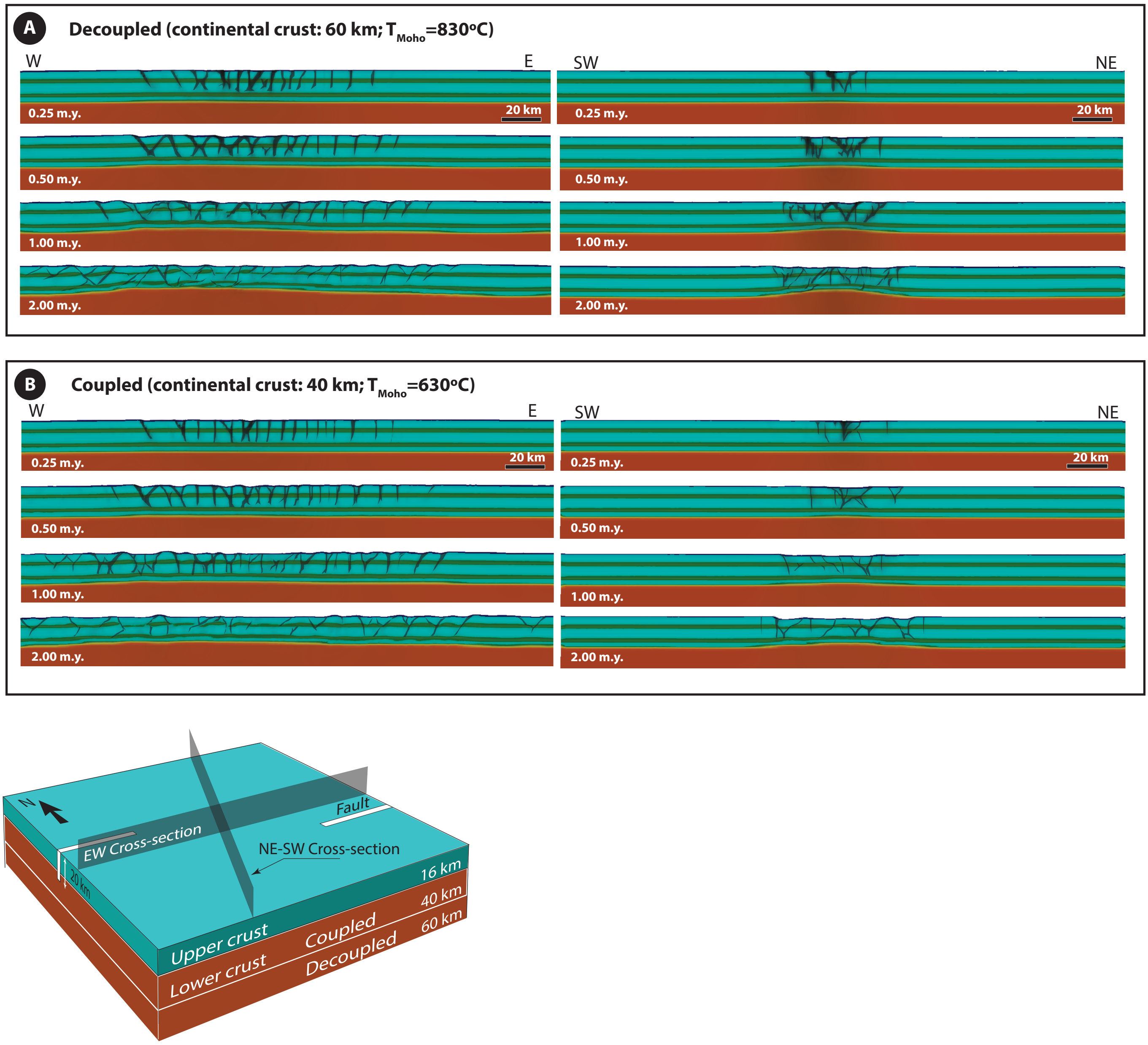

Figure DR1

Rey et al., Gneiss Domes in Pull-Apart

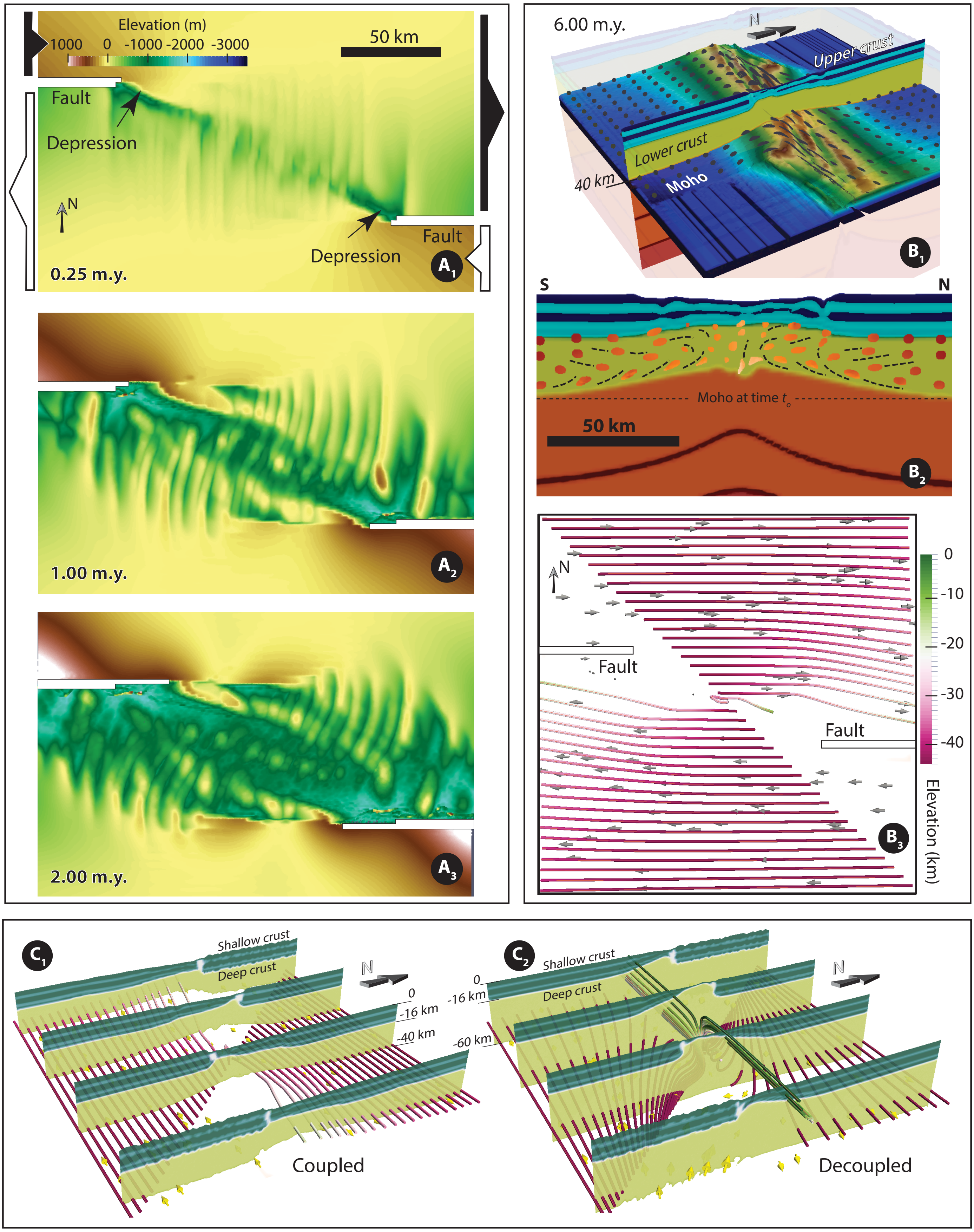

Figure DR2

Rey et al., Gneiss Domes in Pull-Apart

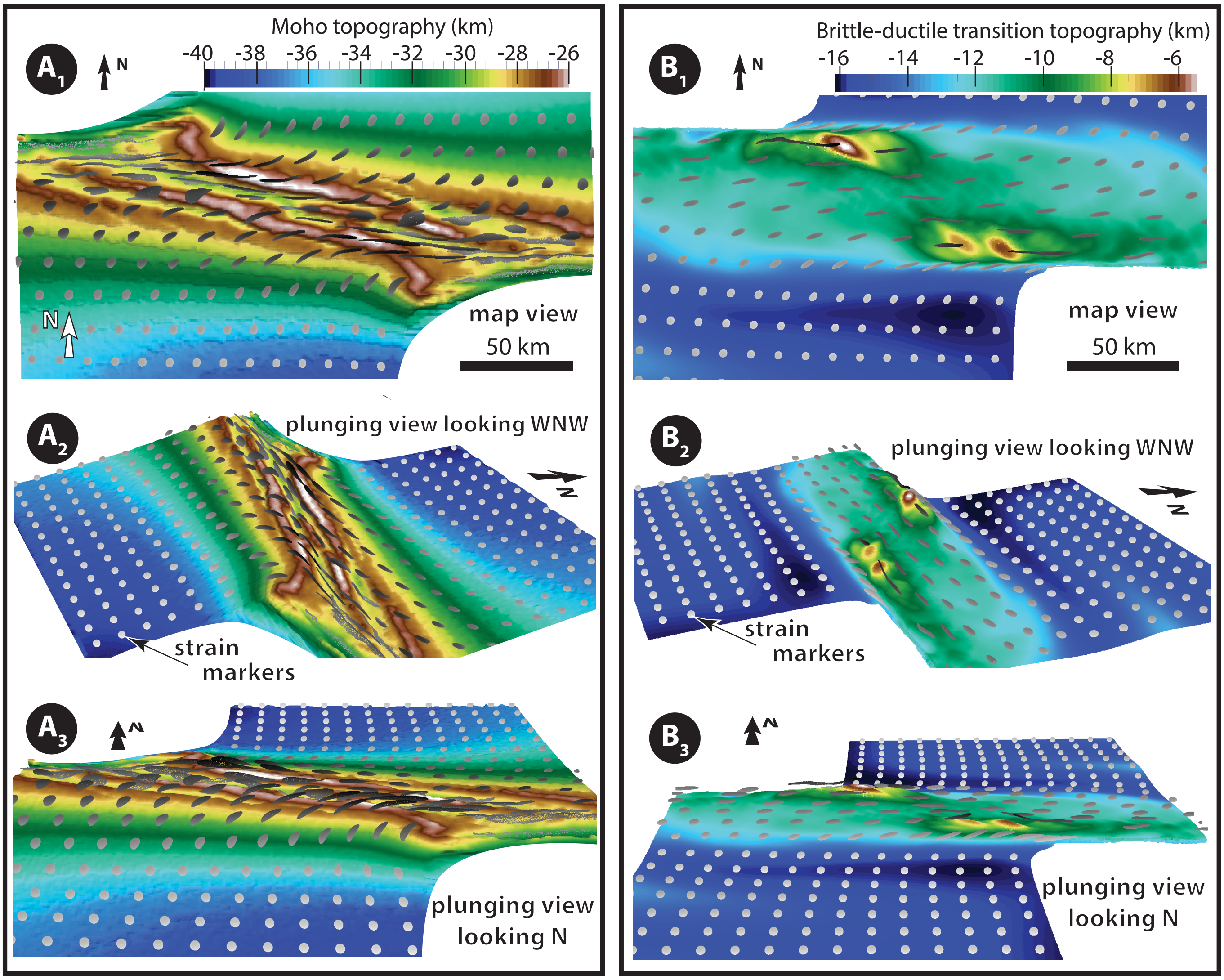

Figure DR3

Rey et al., Gneiss Domes in Pull-Apart

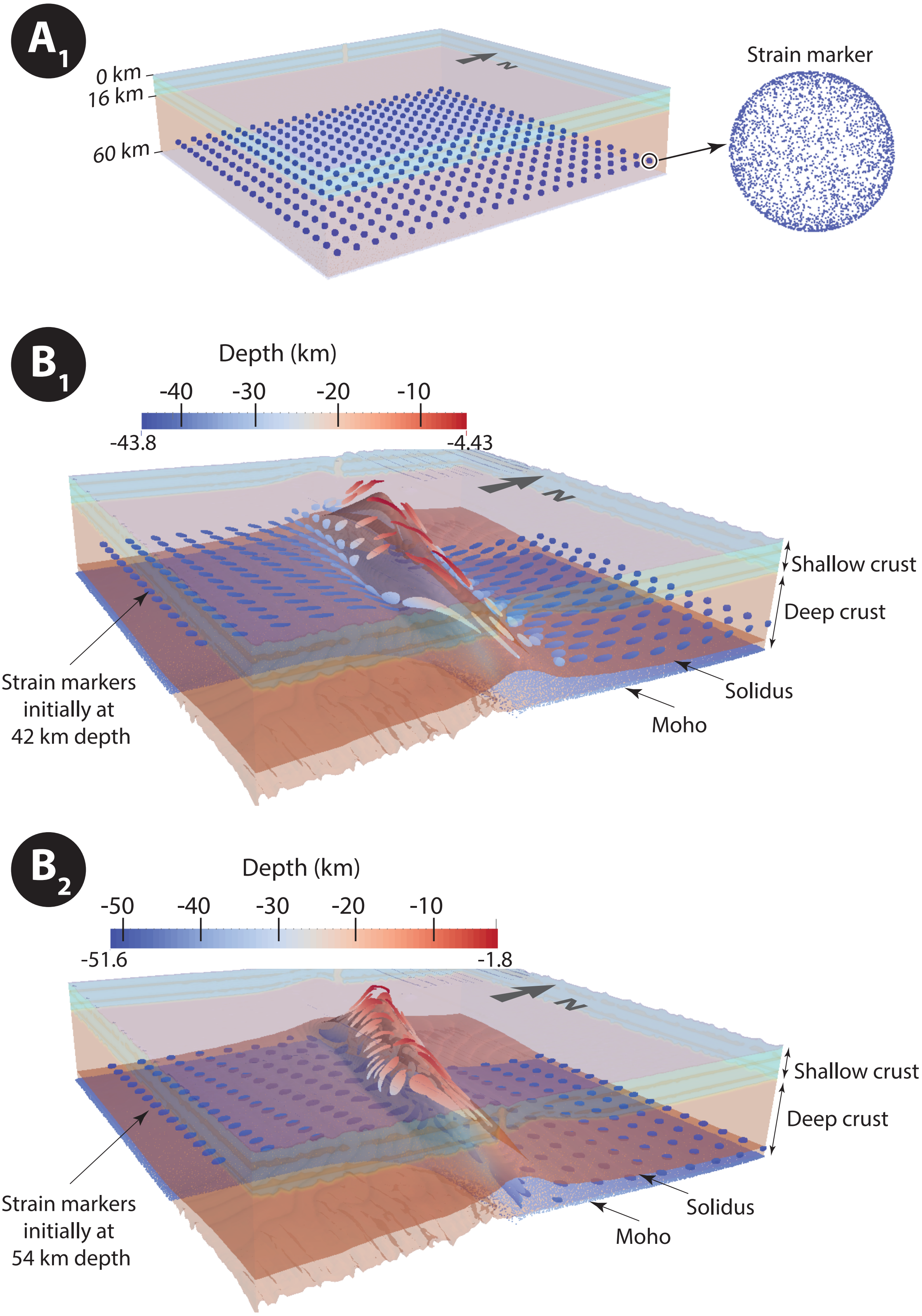

Figure DR4

Rey et al., Gneiss Domes in Pull-Apart